High-momentum-transfer electron scattering from ^{24}Mg, ^{27}Al, ^{28}Si, and ^{32}S†

G. C. Li and M. R. Yearian
High Energy Physics Laboratory and Department of Physics, Stanford University, Stanford, California 94305

I. Sick
High Energy Physics Laboratory, Stanford University, Stanford, California 94305
and Physics Department, University of Basel, Basel, Switzerland

(Received 23 April 1973; revised manuscript received 21 January 1974)

High-momentum-transfer elastic electron scattering data ($0.76 \leq q \leq 3.74$ fm^{-1}) from ^{24}Mg, ^{27}Al, ^{28}Si, and ^{32}S are presented and analyzed using phenomenological charge distributions; the oscillation in $\rho(r)$ due to the shell-model structure is obtained. An analysis in terms of a Woods-Saxon nuclear potential is described and the $2s/1d$ occupation numbers are deduced. The cross sections for certain strongly excited or well isolated inelastic levels are also given, but not analyzed.

[NUCLEAR REACTIONS ^{24}Mg, ^{27}Al, ^{28}Si, ^{32}S (e,e), (e,e'), $E=250$, 500 MeV; measured $\sigma(E,\theta)$, deduced phenomenological ρ; shell-model calculations; deduced $2s/1d$ occupation numbers.]

I. INTRODUCTION

The present paper concerns the investigation of the charge distribution of some s-d shell nuclei by means of elastic electron scattering. The attractiveness of electron scattering lies in the well-known fact of the relatively weak and known electron-nucleus interaction. The electromagnetic properties of the nucleus under consideration can consequently be well separated from the investigation process used. This is especially true for elastic scattering from spin-zero nuclei such as ^{24}Mg, ^{28}Si, and ^{32}S; apart from small corrections (see Sec. IV), the scattering cross section depends exclusively on the ground-state charge distribution. Elastic electron scattering becomes particularly useful at high momentum transfer, since the high momentum transfers reveal the fine details of the shape of the nucleus. Aside from a straightforward folding with the proton size the charge distribution is directly related to the wave function of the protons. Thus a very basic property of the nucleus is determined experimentally.

In a recent electron scattering experiment[1] on Ca for the first time a sufficiently high-momentum-transfer region (3.3 fm^{-1}) was reached so that the cross sections were sensitive to the small variations in the charge density distributions due to shell structure. It was demonstrated in this experiment that in order to explain the measured cross sections at high momentum transfer one could add an oscillation to the Fermi-type charge distribution, which had generally been used previously. The superimposed oscillation produced an additional rise in $\rho(r)$ at small radii. This central rise is easily understood in the framework of the shell model, since it represents the effect of $1s$ and $2s$ shells, which both have their maximum of the wave function at $r=0$. In Ref. 1 it was found, however, that the magnitude of the fluctuation predicted by the shell-model calculation using a Woods-Saxon (WS) potential was in fact larger than the phenomenological (experimental) one. This difference could be due to a deviation of the dominating $2s$-shell contribution from that predicted with the shell-model calculation; recently it was attributed[2] to an incomplete filling of the $2s$ shell through two-particle-two-hole excitations in the doubly magic nucleus ^{40}Ca.

It seemed interesting to investigate more closely the filling of the $2s$ shell, which occurs in the region of $A \sim 24$ to 32 by means of electron scattering at high momentum transfer. Even apart from the question of the filling of the $2s$ shell, this region of A is interesting because of the fact that many calculations assign to these nuclei a rather large deformation, in particular to ^{24}Mg, which would manifest itself in a larger apparent surface thickness than usual.

Elastic electron scattering results from ^{24}Mg, ^{28}Si, and ^{32}S have been obtained previously[3-7] in the range of momentum transfer 0.7 fm$^{-1} \leq q \leq 1.6$ fm^{-1} to determine the phenomenological models of their ground-state charge distributions. Recently, these experiments have been extended up to $q \simeq 2.2$ fm^{-1}.[8-10] The analyses of the data in all cases show that the charge distribution could be represented either by a two-parameter or three-parameter function such as the Fermi distribution. This indicates that the experiments

were not performed at momentum transfers high enough for the oscillatory behavior of the charge distribution predicted by the shell model to appear. In fact, with a simple calculation using a shell model with a harmonic-oscillator potential, it can be shown that the structure in the charge distribution will have significant effects on the elastic electron scattering cross sections only when the momentum transfer q is larger than about 2.1 fm^{-1}.

The dominant influence on the change of the shape of $\rho(r)$ in going from one nucleus to the next in the region $24 \leq A \leq 32$ is the filling of the $2s$ shell, which has the very distinct effect of increasing the charge density at the center of the nucleus; the contribution of a d-shell proton to the central charge density is quite small, since its wave function peaks at $r \cong 3$ fm. If there were no configuration mixing, the filling of the $2s$ shell in the harmonic-oscillator shell model would occur between ^{28}Si and ^{32}S, and yield a considerable increase in $\rho(0)$ from $\sim 0.067\ e\,fm^{-3}$ (^{28}Si) to $\sim 0.117\ e\,fm^{-3}$ (^{32}S) (i.e., a very drastic change of the shape as compared to the very gradual one normally observed when changing Z by 1 or 2). This model also predicts central depressions in $\rho(r)$ for ^{24}Mg and ^{28}Si, and a central rise for ^{32}S. Consequently, it has been the primary purpose of this experiment to extend the measurements of cross sections to a momentum transfer region (3.7 fm^{-1}) which should be high enough to reveal the essential part of this fine structure in $\rho(r)$, and thereby allow direct information to be obtained on the filling of the $2s$ shell.

The aims of the present work have mainly been the *elastic* scattering up to the highest measurable momentum transfer (i.e., of the lowest measurable cross section); no particular effort has been given to studying *inelastic* scattering. The target thickness and the energy spread of the incoming beam have been adjusted for maximum counting rate compatible with proper separation of the elastic peak. Therefore, only the cross sections for certain strongly excited or well isolated inelastic levels could be determined without ambiguity. These cross sections will be given, but not analyzed.

II. EXPERIMENTAL APPARATUS

A beam of electrons of 1–2-μA average current was obtained from the Stanford Mark III accelerator. The energy resolution typical for this experiment was 0.2% full width at half-maximum. To increase the beam current for measurements of low cross sections the energy spread was occasionally increased to 0.3%, provided the elastic peak could still be separated properly.

The momentum of the electron beam was defined by a system of two 30°-deflecting magnets. A complete description of this system is given in Ref. 11. However, the two magnets have since been rebuilt and the energy-defining slits moved from the original symmetrical position.[12] The energy setting of the beam-analyzing magnet was obtained by measuring the magnetic field with a nuclear magnetic resonance probe, which had recently been calibrated to an absolute accuracy of ±0.1% by a floating wire experiment.[13]

The beam was positioned in the scattering chamber by viewing the beam spot on a fluorescent screen with the help of a closed-circuit television system. A spot about 3 mm in diameter was achieved through the use of the pair of quadrupoles localized at the center of the accelerator and by rotation of the pole tips of the second deflecting magnet. In order to keep the scattering angle constant, the beam position at the target was stabilized to ±0.5 mm by using the signal from a split secondary emission monitor (SEM) to regulate the current through the beam steering coils. A screen located 6 m upstream from the target was used to adjust the beam direction along the zero-degree axis of the spectrometer to within ±0.02°.

After passing through the target the beam was stopped in a Faraday cup, and the charge was integrated. At low energies multiple scattering in the target caused some electrons to miss the cup. The collection efficiency was determined by using a SEM upstream from the target to measure the charge ratio of the SEM to the Faraday cup with and without the target.

The electrons scattered from the target were analyzed in momentum by the 183-cm, 180°, $n = -\frac{1}{2}$ double-focusing spectrometer.[14] The spectrometer had a solid angle acceptance of 4.4 msr. The magnetic field in the spectrometer was monitored and stabilized with a rotating coil fluxmeter.[15] The scattering angle had previously been calibrated to ±0.03°. The total angular acceptance in the scattering plane used in the present experiment was ±0.93°. In the vertical direction, where the cross sections and recoil energy vary only very slowly with angle, the acceptance was ±3.9°.

The electrons were detected with a 100-channel detector[16] located in the focal plane of the spectrometer. The 100 plastic detectors spanned a momentum interval $\Delta p/p$ of 9%, the best resolution being ~0.075% per channel. Events were accepted only if they were in fast coincidence with one of the 10 backing-Cerenkov counters, which registered only electrons and, with small ef-

ficiency, pions. With this setup the background at high momentum transfer comes almost exclusively from accidental coincidences between scintillation and Cerenkov counters. Even at the highest q region of this experiment no counts at energies above the elastic peak (i.e., background events) were observed. In between every beam pulse (60 and 120 sec^{-1}) the single and coincidence events were read into a memory which, upon completion of a run, was transferred into an IBM 7700 data-acquisition system, and then stored on a magnetic tape.

The ^{24}Mg and ^{28}Si targets used were isotopically enriched to 99.96% and 98.96%,[17] and had thicknesses of 415 and 446 mg/cm^2, respectively. The thickness and uniformity of the targets were determined to $\pm 1.5\%$ by comparing them with natural Mg and Si sheets through γ-ray absorption measurements. The thickness of the uniform natural targets was determined by measuring the weight and area. The ^{28}Si pressed-powder target was sealed between two thin aluminum foils each 13 mg/cm^2 thick. The small contribution to the scattering cross section due to the aluminum foils was subtracted by using the Al cross section measured with the 403-mg/cm^2-thick Al target.

For the sulfur target the natural isotopic composition (95% ^{32}S) was used. The percentage of the spin $I = \frac{3}{2}$ isotope (0.74% ^{33}S) is too low to give a significant contribution through the high-multipole scattering to the elastic charge cross section. For Mg and Si such high-multipole contributions would have added rather high percentages to the cross section at high momentum transfer, as has been shown in a recent experiment[18] on ^{27}Al. The parameters given in this paper therefore refer to natural sulfur and are expected to be ~0.15% larger than for ^{32}S in the radial parameter. The sulfur target was made in the shape of a disk approximately 8 cm in diameter, and was ground from a cast sulfur piece. Since sulfur tends to crack easily because of thermal tension, a wire was epoxied onto the circumference of the disk in order to hold the target together. The target thickness (405 mg/cm^2) was determined by comparing the sulphur disk with the electron beam at a very low current to a rectangular sulphur piece the thickness of which was determined by weight and area. Due to the extremely poor heat conductivity and low melting point of ^{32}S the use of the maximum beam current available was possible only through rotation of the target, and by adding approximately 10^{-2} atm of H_2 gas into the scattering chamber, which was then separated from the drift tube vacuum by a 10-mg/cm^2-thick aluminum foil. The small amount of H_2 gas served to cool the target by convection; due to the large recoil energy loss of electrons scattered from H, this did not introduce any background events. The steering and integrating SEM, located inside the scattering chamber, was then, with reduced applied voltage, used as an ionization chamber.

In order to calibrate the apparatus, the efficiency of the detection system was determined by measuring the elastic proton cross section using a 480-mg/cm^2-thick polyethylene target. A carbon target with the same number of carbon nuclei per cm^2 as in the CH_2 target was used to determine the carbon background. At both values of the incident energies (250 and 500 MeV) used in this experiment, the efficiency of the system was measured at angles such that the proton elastic peak was well separated from the elastic and discrete inelastic levels of carbon. The efficiency was then determined from the ratio of the experimental proton cross section to the known proton cross section, which was taken from the

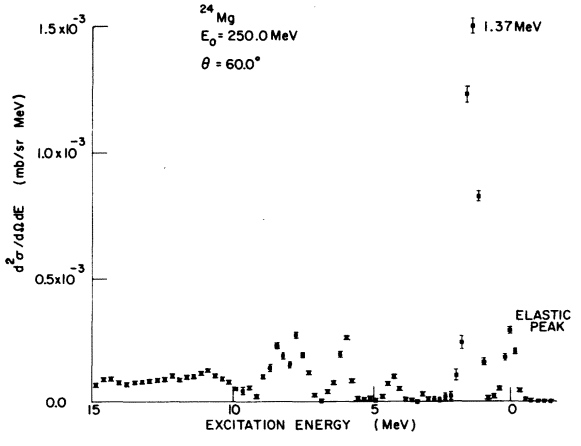

FIG. 1. Unfolded spectrum for ^{24}Mg at 250 MeV and 60°.

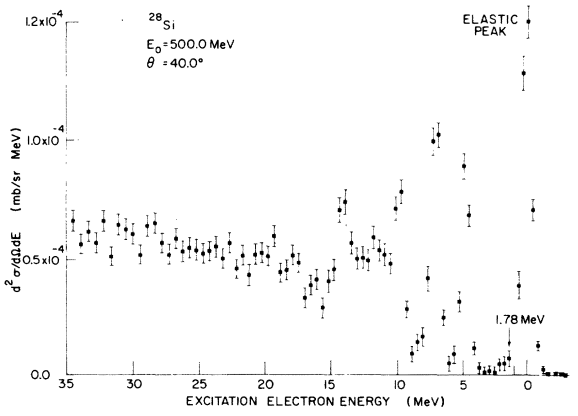

FIG. 2. Unfolded spectrum for ^{28}Si at 500 MeV and 60°.

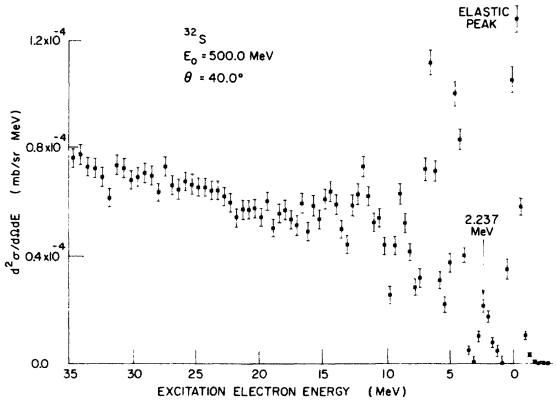

FIG. 3. Unfolded spectrum for ^{32}S at 500 MeV and 60°.

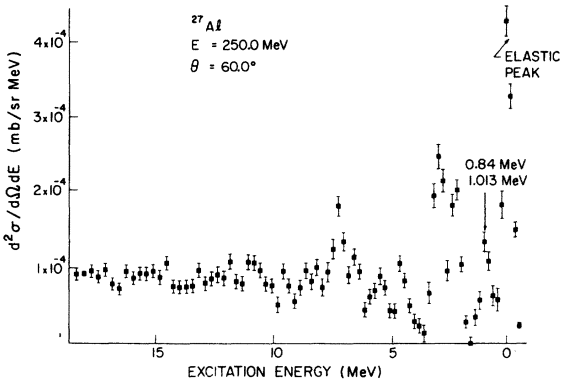

FIG. 4. Unfolded spectrum for ^{27}Al at 250 MeV and 60°.

TABLE I. Elastic cross sections for ^{24}Mg.

E_0 = 250.0 MeV Angle (deg)	Elastic cross sections (mb/sr)	E_0 = 500.0 MeV Angle (deg)	Elastic cross sections (mb/sr)
34	0.269 ± 0.008	34	(0.127 ± 0.004) × 10^{-3}
36	0.167 ± 0.005	36	(0.148 ± 0.004) × 10^{-3}
38	0.102 ± 0.003	38	(0.138 ± 0.004) × 10^{-3}
40	(0.637 ± 0.019) × 10^{-1}	40	(0.107 ± 0.003) × 10^{-3}
42	(0.389 ± 0.012) × 10^{-1}	42	(0.697 ± 0.021) × 10^{-4}
44	(0.231 ± 0.007) × 10^{-1}	44	(0.408 ± 0.012) × 10^{-4}
46	(0.143 ± 0.004) × 10^{-1}	46	(0.241 ± 0.007) × 10^{-4}
48	(0.792 ± 0.024) × 10^{-2}	48	(0.111 ± 0.003) × 10^{-4}
50	(0.477 ± 0.014) × 10^{-2}	50	(0.503 ± 0.015) × 10^{-5}
52	(0.250 ± 0.008) × 10^{-2}	52	(0.204 ± 0.008) × 10^{-5}
54	(0.141 ± 0.004) × 10^{-2}	54	(0.725 ± 0.046) × 10^{-6}
56	(0.677 ± 0.021) × 10^{-3}	56	(0.222 ± 0.022) × 10^{-6}
58	(0.344 ± 0.010) × 10^{-3}	58	(0.468 ± 0.105) × 10^{-7}
60	(0.163 ± 0.005) × 10^{-3}	60	(0.279 ± 0.073) × 10^{-7}
62	(0.695 ± 0.021) × 10^{-4}	64	(0.271 ± 0.054) × 10^{-7}
64	(0.308 ± 0.009) × 10^{-4}	66	(0.157 ± 0.027) × 10^{-7}
66	(0.214 ± 0.006) × 10^{-4}	68	(0.133 ± 0.035) × 10^{-7}
68	(0.226 ± 0.007) × 10^{-4}	70	(0.779 ± 0.180) × 10^{-8}
70	(0.262 ± 0.008) × 10^{-4}	72	(0.547 ± 0.150) × 10^{-8}
72	(0.286 ± 0.009) × 10^{-4}	74	(0.540 ± 0.146) × 10^{-8}
74	(0.316 ± 0.010) × 10^{-4}	78	(0.274 ± 0.115) × 10^{-8}
76	(0.309 ± 0.009) × 10^{-4}	82	(0.270 ± 0.110) × 10^{-8}
78	(0.299 ± 0.009) × 10^{-4}	86	(0.192 ± 0.080) × 10^{-8}
80	(0.255 ± 0.008) × 10^{-4}		
82	(0.240 ± 0.007) × 10^{-4}		
84	(0.207 ± 0.006) × 10^{-4}		
86	(0.181 ± 0.005) × 10^{-4}		
88	(0.143 ± 0.004) × 10^{-4}		
90	(0.118 ± 0.004) × 10^{-4}		
92	(0.910 ± 0.027) × 10^{-5}		
94	(0.790 ± 0.024) × 10^{-5}		
98	(0.450 ± 0.014) × 10^{-5}		
102	(0.277 ± 0.008) × 10^{-5}		
106	(0.163 ± 0.006) × 10^{-5}		
110	(0.823 ± 0.038) × 10^{-6}		

TABLE II. Elastic cross sections for ^{28}Si.

E_0 = 250.0 MeV Angle (deg)	Elastic cross sections (mb/sr)	E_0 = 500.0 MeV Angle (deg)	Elastic cross sections (mb/sr)
34	0.293 ± 0.009	34	(0.328 ± 0.010) × 10^{-3}
36	0.178 ± 0.005	35	(0.323 ± 0.010) × 10^{-3}
38	0.107 ± 0.003	36	(0.319 ± 0.010) × 10^{-3}
40	(0.660 ± 0.020) × 10^{-1}	38	(0.224 ± 0.007) × 10^{-3}
42	(0.390 ± 0.012) × 10^{-1}	40	(0.155 ± 0.005) × 10^{-3}
44	(0.245 ± 0.007) × 10^{-1}	42	(0.900 ± 0.027) × 10^{-4}
46	(0.132 ± 0.004) × 10^{-1}	44	(0.502 ± 0.015) × 10^{-4}
48	(0.760 ± 0.023) × 10^{-2}	46	(0.250 ± 0.008) × 10^{-4}
50	(0.396 ± 0.012) × 10^{-2}	48	(0.104 ± 0.003) × 10^{-4}
52	(0.213 ± 0.006) × 10^{-2}	50	(0.344 ± 0.011) × 10^{-5}
54	(0.100 ± 0.003) × 10^{-2}	52	(0.127 ± 0.006) × 10^{-5}
56	(0.500 ± 0.015) × 10^{-3}	54	(0.262 ± 0.021) × 10^{-6}
58	(0.215 ± 0.006) × 10^{-3}	56	(0.749 ± 0.112) × 10^{-7}
60	(0.998 ± 0.030) × 10^{-4}	60	(0.154 ± 0.016) × 10^{-6}
62	(0.617 ± 0.019) × 10^{-4}	62	(0.168 ± 0.018) × 10^{-6}
64	(0.550 ± 0.017) × 10^{-4}	64	(0.109 ± 0.016) × 10^{-6}
66	(0.622 ± 0.019) × 10^{-4}	66	(0.750 ± 0.072) × 10^{-7}
68	(0.660 ± 0.020) × 10^{-4}	68	(0.761 ± 0.095) × 10^{-7}
70	(0.710 ± 0.021) × 10^{-4}	70	(0.382 ± 0.080) × 10^{-7}
72	(0.685 ± 0.021) × 10^{-4}	74	(0.102 ± 0.021) × 10^{-7}
74	(0.655 ± 0.020) × 10^{-4}	78	(0.362 ± 0.152) × 10^{-8}
76	(0.580 ± 0.017) × 10^{-4}	82	(0.272 ± 0.216) × 10^{-9}
78	(0.542 ± 0.016) × 10^{-4}	90	(0.127 ± 0.074) × 10^{-9}
80	(0.461 ± 0.014) × 10^{-4}	94	(0.101 ± 0.074) × 10^{-9}
82	(0.387 ± 0.012) × 10^{-4}		
84	(0.310 ± 0.009) × 10^{-4}		
86	(0.255 ± 0.008) × 10^{-4}		
88	(0.198 ± 0.006) × 10^{-4}		
90	(0.153 ± 0.005) × 10^{-4}		
92	(0.124 ± 0.004) × 10^{-4}		
94	(0.932 ± 0.028) × 10^{-5}		
98	(0.508 ± 0.015) × 10^{-5}		
102	(0.275 ± 0.008) × 10^{-5}		
106	(0.128 ± 0.005) × 10^{-5}		
110	(0.638 ± 0.036) × 10^{-6}		

absolute measurements of Ref. 19. The measured efficiency was usually a few percent below 1.0.

III. EXPERIMENTAL RESULTS

In the analysis of the data obtained from the 100-channel ladder several corrections were necessary. After the dead-time corrections (at maximum 10%) the spectra were adjusted for the relative efficiencies of the 100-channel detectors, which differed by a few percent from detector to detector. The relative efficiencies were obtained by taking several overlapping spectra of the smooth quasielastic peak. The total momentum interval spanned by the series of spectra was chosen to be about twice the momentum acceptance of the spectrometer. Since the quasielastic spectrum is a smooth and slowly varying function of the scattered energy, the deviation of each individual channel from a polynomial best fit to these spectra give the relative efficiencies of the plastic detectors.[20]

The most significant correction that must be applied to the data is the unfolding of the radiative tail. The unfolding procedure included in the cross section those electrons that lost enough energy to fall outside the peak in question. The radiative effects considered here were: bremsstrahlung emission due to the finite target thickness, emission due to the scattering from a nucleus (Schwinger radiation), and Landau straggling. The unfolding was performed with an improved version of the program originally described in Ref. 21. The unfolding of the three effects mentioned was done channel by channel, starting at the highest electron energy. This procedure yields elastic and inelastic peaks with all the radiative tails removed. For cases where the elastic peak was well separated from inelastic peaks the procedure was checked by comparing the result with that obtained by using the more accurate formula of Ref. 22. We found the cross sections to be the same within ±2%. Some typical unfolded spectra are given in Figs. 1–4.

In the cases where the elastic peak was clearly separated from the inelastic ones the cross section was obtained by integrating the area under the unfolded elastic peak between two given limits. For the extraction of the inelastic cross sections a curve fitting program was used to decompose the spectrum into separate Gaussians, the width of which was determined by the elastic peak. If the excitation energies of the levels were known they were used as constraints for the fits. The curve-fitting procedure was also applied in the case of the elastic cross sections of ^{24}Mg in the neighborhood of the second diffraction minimum, where the separation from the very dominant scattering from the 1.37-MeV 2^+ level was not possible by choosing a cutoff.

The elastic cross sections of ^{27}Al were obtained from the measured ^{27}Al data which were necessary for the background subtraction of the ^{28}Si pressed-powder target, which was encased in two thin aluminum foils. For the determination of the ^{27}Al elastic cross section the shape and position of the peaks were obtained from the ^{32}S elastic peak which was measured alternately with ^{27}Al. Due to these constraints the extraction of the ^{27}Al elastic cross section is quite precise even if the elastic peak was not separated from the 0.842- and 1.011-MeV levels. No phenomenological analysis has yet been made for these ^{27}Al elastic cross sections. This is primarily due to the necessity of treating the higher multipole contributions to the charge

TABLE III. Elastic cross sections for S.

$E_0 = 250.0$ MeV		$E_0 = 500.0$ MeV	
Angle (deg)	Elastic cross sections (mb/sr)	Angle (deg)	Elastic cross sections (mb/sr)
34	0.328 ± 0.010	34	$(0.498 \pm 0.015) \times 10^{-3}$
36	0.193 ± 0.006	35	$(0.446 \pm 0.013) \times 10^{-3}$
38	0.113 ± 0.003	36	$(0.373 \pm 0.010) \times 10^{-3}$
40	$(0.687 \pm 0.021) \times 10^{-1}$	38	$(0.257 \pm 0.008) \times 10^{-3}$
42	$(0.384 \pm 0.011) \times 10^{-1}$	40	$(0.134 \pm 0.004) \times 10^{-3}$
44	$(0.218 \pm 0.006) \times 10^{-1}$	42	$(0.639 \pm 0.019) \times 10^{-4}$
46	$(0.118 \pm 0.004) \times 10^{-1}$	44	$(0.276 \pm 0.008) \times 10^{-4}$
48	$(0.599 \pm 0.018) \times 10^{-2}$	46	$(0.106 \pm 0.003) \times 10^{-4}$
50	$(0.288 \pm 0.009) \times 10^{-2}$	48	$(0.272 \pm 0.012) \times 10^{-5}$
52	$(0.143 \pm 0.004) \times 10^{-2}$	50	$(0.591 \pm 0.038) \times 10^{-6}$
54	$(0.637 \pm 0.019) \times 10^{-3}$	52	$(0.281 \pm 0.026) \times 10^{-6}$
56	$(0.280 \pm 0.008) \times 10^{-3}$	54	$(0.416 \pm 0.038) \times 10^{-6}$
58	$(0.148 \pm 0.004) \times 10^{-3}$	56	$(0.524 \pm 0.043) \times 10^{-6}$
60	$(0.107 \pm 0.003) \times 10^{-3}$	58	$(0.495 \pm 0.040) \times 10^{-6}$
62	$(0.104 \pm 0.003) \times 10^{-3}$	60	$(0.409 \pm 0.031) \times 10^{-6}$
64	$(0.114 \pm 0.003) \times 10^{-3}$	62	$(0.328 \pm 0.030) \times 10^{-6}$
66	$(0.121 \pm 0.004) \times 10^{-3}$	64	$(0.170 \pm 0.015) \times 10^{-6}$
68	$(0.119 \pm 0.004) \times 10^{-3}$	66	$(0.104 \pm 0.008) \times 10^{-6}$
70	$(0.118 \pm 0.004) \times 10^{-3}$	68	$(0.485 \pm 0.054) \times 10^{-7}$
72	$(0.104 \pm 0.003) \times 10^{-3}$	70	$(0.362 \pm 0.046) \times 10^{-7}$
74	$(0.905 \pm 0.027) \times 10^{-4}$	74	$(0.585 \pm 0.163) \times 10^{-8}$
76	$(0.699 \pm 0.021) \times 10^{-4}$	78	$(0.140 \pm 0.057) \times 10^{-8}$
78	$(0.618 \pm 0.019) \times 10^{-4}$	82	$(0.397 \pm 0.204) \times 10^{-9}$
80	$(0.467 \pm 0.014) \times 10^{-4}$	90	$(0.217 \pm 0.089) \times 10^{-9}$
82	$(0.366 \pm 0.011) \times 10^{-4}$	94	$(0.115 \pm 0.091) \times 10^{-9}$
84	$(0.272 \pm 0.008) \times 10^{-4}$		
86	$(0.201 \pm 0.006) \times 10^{-4}$		
88	$(0.150 \pm 0.005) \times 10^{-4}$		
90	$(0.106 \pm 0.003) \times 10^{-4}$		
92	$(0.751 \pm 0.023) \times 10^{-5}$		
94	$(0.525 \pm 0.016) \times 10^{-5}$		
98	$(0.232 \pm 0.010) \times 10^{-5}$		
102	$(0.945 \pm 0.047) \times 10^{-6}$		
106	$(0.320 \pm 0.028) \times 10^{-6}$		
110	$(0.108 \pm 0.013) \times 10^{-6}$		

TABLE IV. Elastic cross sections for ^{27}Al.

E_0 = 250.0 MeV Angle (deg)	Elastic cross sections (mb/sr)	E_0 = 500.0 MeV Angle (deg)	Elastic cross sections (mb/sr)
34	0.278 ± 0.008	34	$(0.364 \pm 0.012) \times 10^{-3}$
36	0.179 ± 0.005	35	$(0.375 \pm 0.011) \times 10^{-3}$
38	0.116 ± 0.003	36	$(0.354 \pm 0.011) \times 10^{-3}$
40	$(0.705 \pm 0.021) \times 10^{-1}$	38	$(0.270 \pm 0.008) \times 10^{-3}$
42	$(0.437 \pm 0.013) \times 10^{-1}$	40	$(0.190 \pm 0.006) \times 10^{-3}$
44	$(0.265 \pm 0.008) \times 10^{-1}$	42	$(0.125 \pm 0.004) \times 10^{-3}$
46	$(0.155 \pm 0.005) \times 10^{-1}$	44	$(0.752 \pm 0.020) \times 10^{-4}$
48	$(0.876 \pm 0.026) \times 10^{-2}$	46	$(0.445 \pm 0.013) \times 10^{-4}$
50	$(0.515 \pm 0.015) \times 10^{-2}$	48	$(0.204 \pm 0.006) \times 10^{-4}$
52	$(0.286 \pm 0.009) \times 10^{-2}$	50	$(0.108 \pm 0.008) \times 10^{-4}$
54	$(0.153 \pm 0.005) \times 10^{-2}$	52	$(0.499 \pm 0.049) \times 10^{-5}$
56	$(0.770 \pm 0.023) \times 10^{-3}$	54	$(0.255 \pm 0.026) \times 10^{-5}$
58	$(0.412 \pm 0.012) \times 10^{-3}$	56	$(0.156 \pm 0.016) \times 10^{-5}$
60	$(0.236 \pm 0.007) \times 10^{-3}$	58	$(0.887 \pm 0.089) \times 10^{-6}$
62	$(0.139 \pm 0.004) \times 10^{-3}$	60	$(0.510 \pm 0.051) \times 10^{-6}$
64	$(0.101 \pm 0.003) \times 10^{-3}$	62	$(0.326 \pm 0.033) \times 10^{-6}$
66	$(0.850 \pm 0.026) \times 10^{-4}$	64	$(0.173 \pm 0.017) \times 10^{-6}$
68	$(0.862 \pm 0.026) \times 10^{-4}$	66	$(0.160 \pm 0.016) \times 10^{-6}$
70	$(0.835 \pm 0.025) \times 10^{-4}$	68	$(0.778 \pm 0.078) \times 10^{-7}$
72	$(0.820 \pm 0.025) \times 10^{-4}$	70	$(0.285 \pm 0.041) \times 10^{-7}$
74	$(0.795 \pm 0.024) \times 10^{-4}$		
76	$(0.710 \pm 0.021) \times 10^{-4}$		
78	$(0.613 \pm 0.018) \times 10^{-4}$		
80	$(0.542 \pm 0.016) \times 10^{-4}$		
82	$(0.464 \pm 0.014) \times 10^{-4}$		
84	$(0.374 \pm 0.012) \times 10^{-4}$		
86	$(0.314 \pm 0.009) \times 10^{-4}$		
88	$(0.260 \pm 0.008) \times 10^{-4}$		
90	$(0.219 \pm 0.007) \times 10^{-4}$		
92	$(0.162 \pm 0.005) \times 10^{-4}$		
94	$(0.144 \pm 0.004) \times 10^{-4}$		
98	$(0.776 \pm 0.023) \times 10^{-5}$		
102	$(0.526 \pm 0.016) \times 10^{-5}$		
106	$(0.326 \pm 0.011) \times 10^{-5}$		
110	$(0.204 \pm 0.067) \times 10^{-5}$		
114	$(0.124 \pm 0.038) \times 10^{-5}$		
118	$(0.803 \pm 0.032) \times 10^{-6}$		
122	$(0.655 \pm 0.034) \times 10^{-6}$		
126	$(0.400 \pm 0.019) \times 10^{-6}$		

E_0 (MeV)	Angle (deg)	Elastic cross sections (mb/sr)
170.0	135.0	$(0.805 \pm 0.080) \times 10^{-5}$
188.5	135.0	$(0.450 \pm 0.045) \times 10^{-5}$
195.0	135.0	$(0.332 \pm 0.020) \times 10^{-5}$
204.5	122.6	$(0.600 \pm 0.060) \times 10^{-5}$
221.0	104.0	$(0.147 \pm 0.015) \times 10^{-4}$
221.0	135.0	$(0.915 \pm 0.092) \times 10^{-6}$
254.0	135.0	$(0.200 \pm 0.020) \times 10^{-6}$
270.0	135.0	$(0.114 \pm 0.011) \times 10^{-6}$
285.5	135.0	$(0.128 \pm 0.013) \times 10^{-6}$

scattering in ^{27}Al. The contributions from magnetic scattering have been extracted before and analyzed in Refs. 18 and 23.

The elastic cross sections for ^{24}Mg, ^{28}Si, S, and ^{27}Al measured in this experiment are presented in Tables I–IV and in Figs. 5–8. The data were taken at two incident energies, 250 and 500 MeV, referred to the center of the target for each nucleus in order to cover the desired range of momentum transfer. No data were taken at angles below 34°; accurate cross sections were harder to obtain at those angles with our apparatus, since for small angles the low beam current must be integrated with a SEM rather than the Faraday cup. The high-momentum-transfer data were all taken at 500 MeV, since at a given value of q the cross section is approximately proportional to the square of the incident energy E_0.

The uncertainty in incident energy was ±0.1% and the reproducibility was about ±0.03%. The systematic error common to all cross sections at one incident energy was ±3%, and was due mainly to the uncertainty in the absolute hydrogen cross section used to calibrate our apparatus. The errors shown in Tables I–IV are statistical errors only.

The inelastic cross sections of the low-lying levels for ^{24}Mg, ^{28}Si, and ^{32}S measured in this experiment are given in Figs. 9–14 without an analysis in terms of phenomenological transition

charge densities. They are shown because in the literature there are very few high-q inelastic form factors available for comparison with theoretical calculations.

IV. EMPIRICAL CHARGE DISTRIBUTIONS

The nuclei considered here, ^{24}Mg, ^{28}Si, and ^{32}S, all have zero spin. Therefore the elastic cross sections are determined purely by the ground-state charge distribution. In the first Born approximation, which applies to nuclei with $Z\alpha \ll 1$, the charge distribution is simply the Fourier transform of the form factor and vice versa. That is,

$$\rho(r) = \frac{Ze}{2\pi^2 r} \int_0^\infty F(q)\sin(qr) q\, dq \tag{1}$$

and

$$F(q) = \frac{1}{Zeq} \int_0^\infty \rho(r)\sin(qr) 4\pi r\, dr\,. \tag{2}$$

In our case $Z\alpha$ is not $\ll 1$, so that while the application of plane-wave Born approximation is a valuable tool for obtaining qualitative ideas, it is not adequate for a quantitative analysis. With the present data, Eq. (1) tells us that the experiment will only give the Fourier components of $\rho(r)$ with a wave length larger than $2\pi/q_{max} \simeq 1.6$ fm.

Since $Z\alpha$ is not much less than unity, the exact phase-shift calculation was used to analyze the data of the experiment. The phase-shift program[24] used was based on the method described in Ref. 25; it allows one to solve the Dirac equation numerically for the electron in the Coulomb field of the nucleus.

The general procedure was to try to find a phenomenological charge distribution which, when used with the phase-shift program, gave the observed cross sections. Since the high-momentum-transfer behavior of $F(q)$ is unknown, one starts with the simplest possible smooth charge distribution $\rho_0(r)$ and then adds a minimum amount of higher-frequency components necessary to explain the measured experimental cross sections. The approach in fitting was therefore to first fit the data up to the maximum momentum transfer compatible with a good fit using one of the standard phenomenological model [e.g., a three-parameter Fermi (3pF) or a three-parameter Gaussian (3pG)

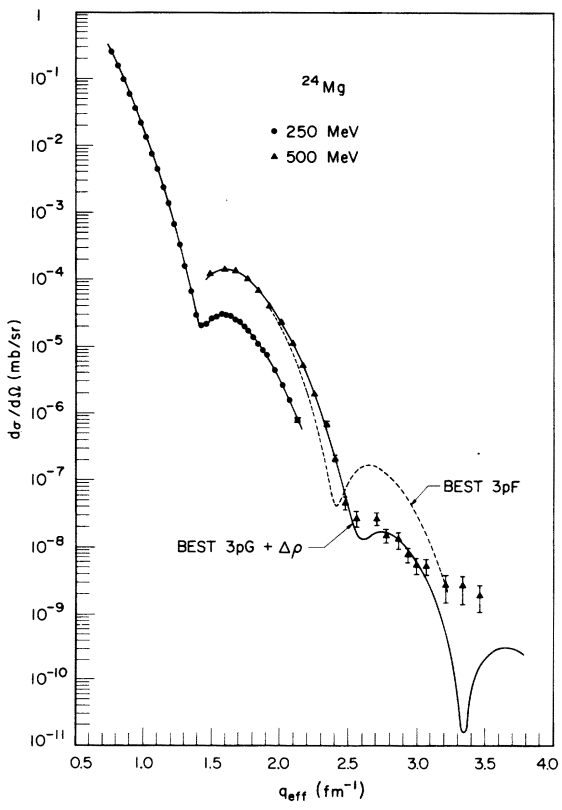

FIG. 5. Experimental elastic cross sections from ^{24}Mg and best phenomenological fit.

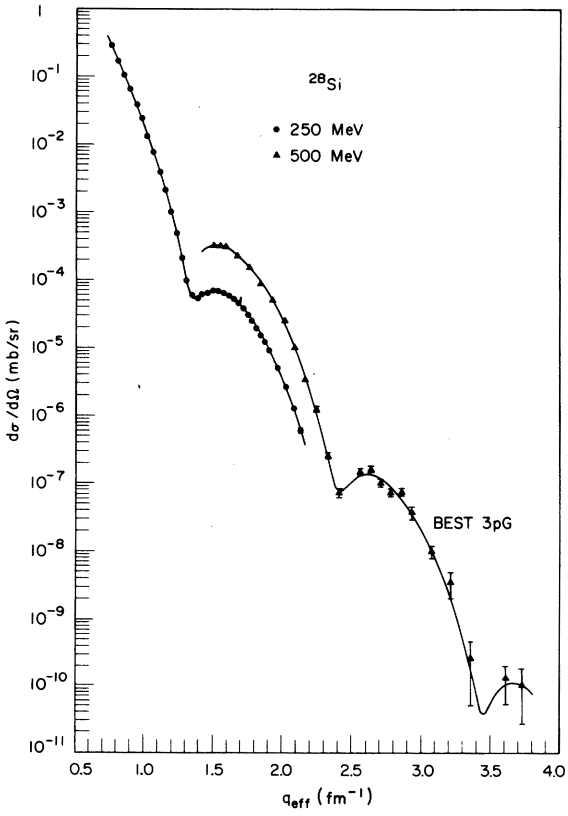

FIG. 6. Experimental elastic cross sections from ^{28}Si and best phenomenological fit.

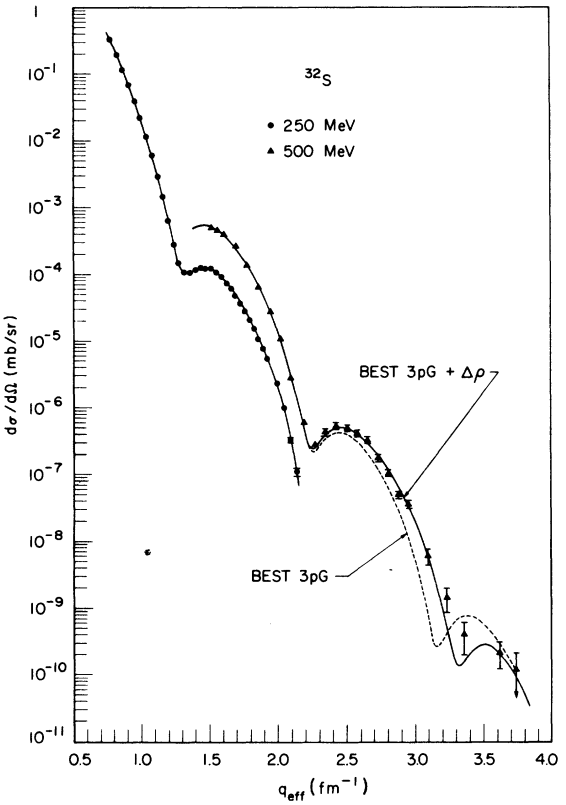

FIG. 7. Experimental elastic cross sections from S and best phenomenological fit.

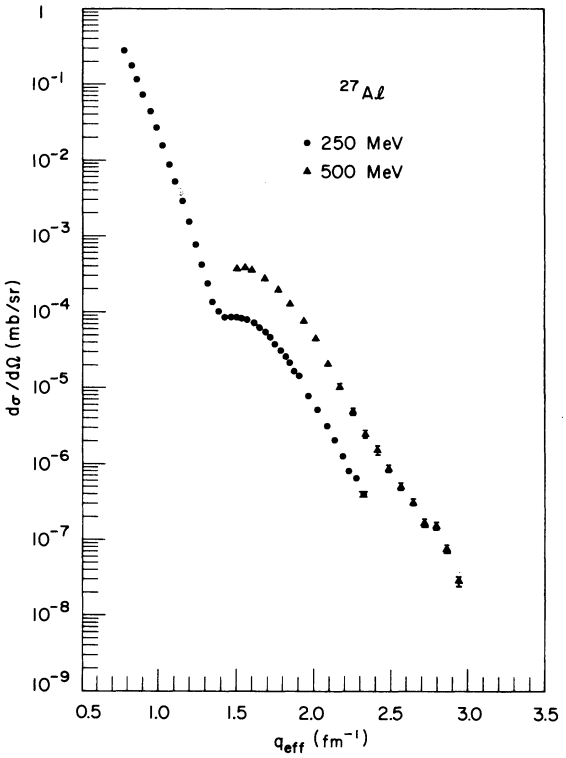

FIG. 8. Experimental elastic cross sections from ^{27}Al.

distribution]. The q region roughly corresponds to the range of the 250-MeV data ($q < 2.1$ fm^{-1}). Then, if necessary, a modification $\Delta\rho$ was added to explain the rest of the high-q data. The shape of the modification used, a damped oscillation, is such that the low-q fit is virtually not influenced by it; the parameters of the basic distribution ρ_0 are therefore almost independent of $\Delta\rho$. The weak correlation was accounted for by iterating several times in performing successive fits of ρ_0 and $\Delta\rho$.

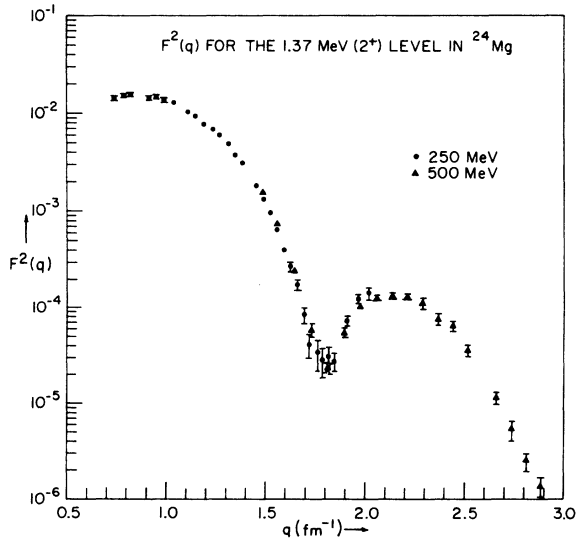

FIG. 9. Experimental form factor of the 1.37-MeV (2^+) level in ^{24}Mg.

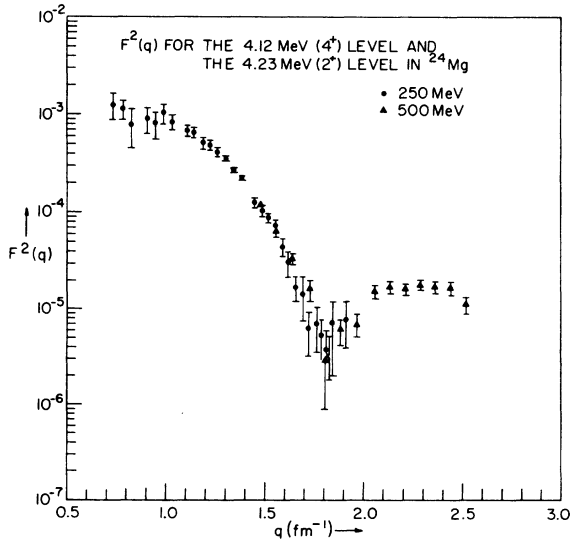

FIG. 10. Experimental form factor of the 4.12-MeV (4^+) and the 4.23-MeV (2^+) levels in ^{24}Mg.

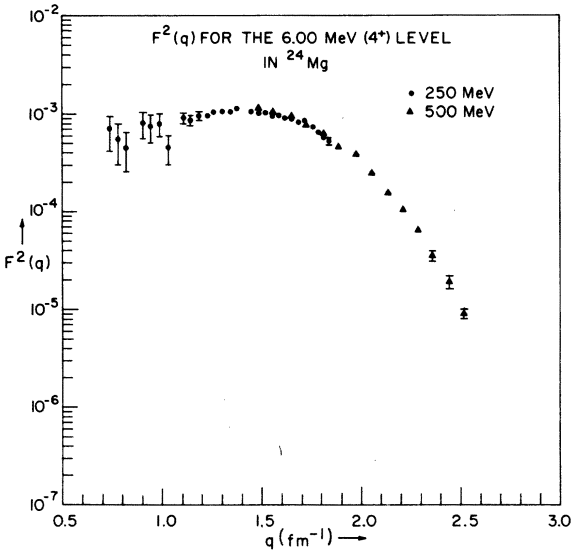

FIG. 11. Experimental form factor of the 6.00-MeV (4^+) level in ^{24}Mg.

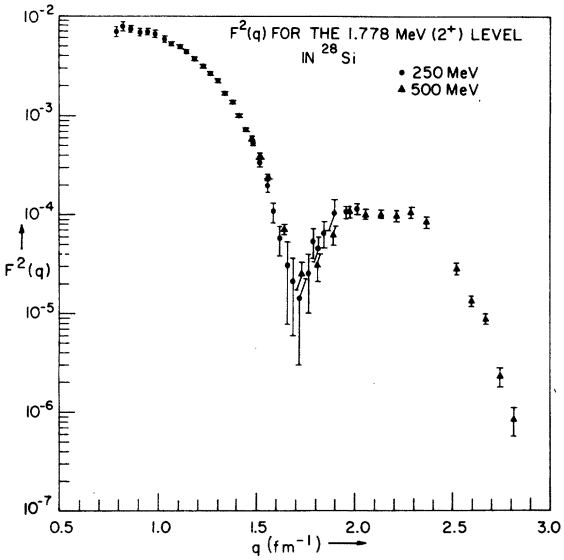

FIG. 12. Experimental form factor of the 1.778-MeV (2^+) level in ^{28}Si.

This procedure is more transparent than the fits which vary all the parameters simultaneously. Some of the data have also been fitted by the latter method, which produces the same χ^2 and parameters different by less than their errors.

The analytical shapes used to fit the low-q part of the data, which comprises differential cross sections with experimental errors of $\pm 3\%$, are the three-parameter Fermi or Gaussian distributions

$$\rho_0(r) \propto (1+wr^2/c^2)/\left[1+\exp\left(\frac{r^n-c^n}{z^n}\right)\right] \quad n=1,2\,. \tag{3}$$

These distributions have three adjustable parameters: the half-density radius c, skin thickness z, and w which serves in light nuclei essentially to influence the tail of $\rho(r)$.

At the higher momentum transfers the experimental cross sections and the fit using ρ_0 generally differ since ρ_0 does not have the necessary flexibility. Usually this difference shows as a function of q a roughly symmetrical peak with a width of 1 fm^{-1}. A convenient parametrization able to produce the desired change in cross section is[1]

$$\Delta\rho(r) = A\rho_0(0)\left(\frac{\sin q_0 r}{q_0 r} + \frac{p^2}{2q_0^2}\cos q_0 r\right) e^{-p^2 r^2/4}\,, \tag{4}$$

where A, q_0, and p are three new adjustable parameters. In Born approximation it can be easily seen that the resulting form factor is

$$\Delta F(q) = A' \exp\left[-\left(\frac{q-q_0}{p}\right)^2\right]\,. \tag{5}$$

The shape of these modifications does, of course, depend on the choice of ρ_0.

^{24}Mg

A good fit to the ^{24}Mg data is obtainable with the 3pF model up to $q \sim 2.1$ fm^{-1}; this fit is shown in Fig. 5. At the high momentum transfers the calculated second diffraction minimum occurs at too low a value of q. The difference between the experimental and the best 3pF fit over the region 2.1–3.3 fm^{-1} looks roughly like a Gaussian as a

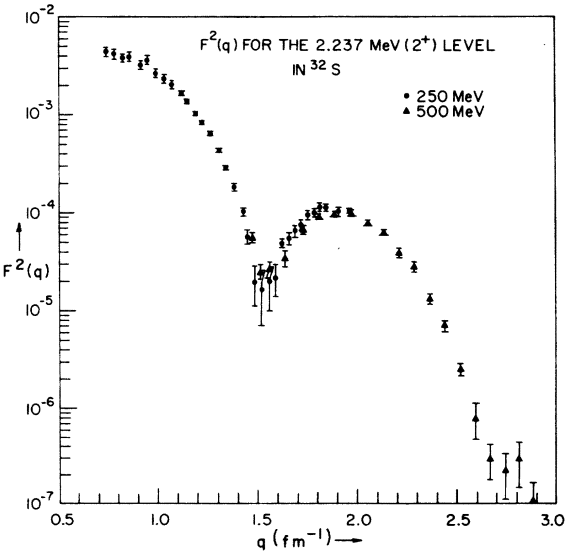

FIG. 13. Experimental form factor of the 2.237-MeV (2^+) level in ^{32}S.

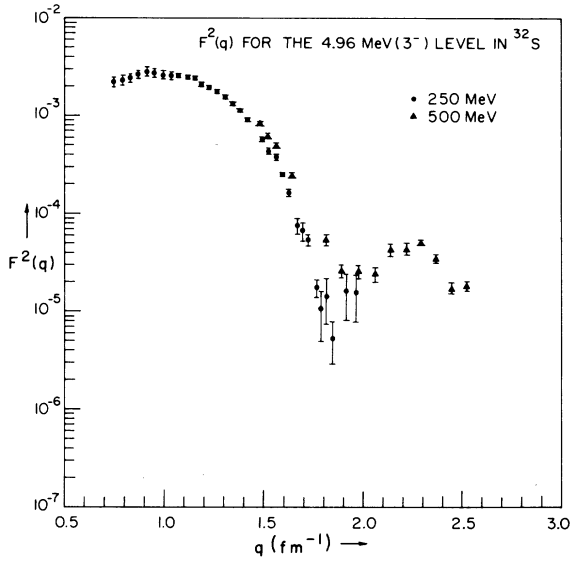

FIG. 14. Experimental form factor of the 4.96-MeV (3^-) level in ^{32}S.

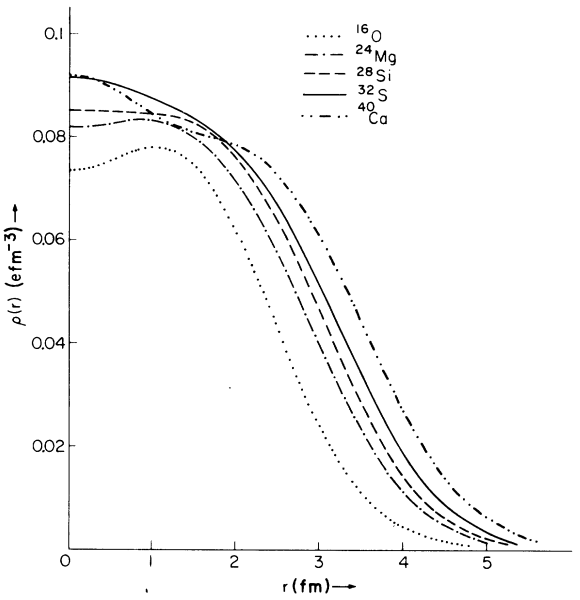

FIG. 15. Best-fit charge distributions; ^{16}O and ^{40}Ca densities are from Refs. 26 and 1.

function of momentum transfer and therefore can be eliminated by adding to the 3pF distribution (ρ_0) a modification of the shape (4). The best fit using $\rho = \rho_0 + \Delta\rho$ has a χ^2 of 1.5 per degree of freedom. The corresponding charge distribution is displayed in Fig. 15. The parameters are given in Table V. The 3pG model does not in this case give as good a fit; using one modification, the best χ^2 obtained is 7.8 per degree of freedom.

^{28}Si

In the case of ^{28}Si, the 3pF model gives an acceptable fit to the low-q data, even though the χ^2 using 3pG is somewhat better. At the higher momentum transfer ($q \geq 2$ fm^{-1}) the situation is quite complicated, since the difference between experiment and fit shows more structure than can be accounted for with Eq. (4); a more flexible function would be needed. Two successive modifications of the shape described by Eq. (4), allows one to fit the data without considerable systematic deviations ($\chi^2 = 2.2$ per degree of freedom) but at the expense of adding more adjustable parameters. The 3pG model is much better adapted to the ^{28}Si charge distribution, since it fits the data up to the highest momentum transfers. The small residual systematic deviations of fit and data do not warrant the introduction of a modification. The best fit has a χ^2 of 1.6 per degree of freedom and is given in Figs. 6 and 15.

^{32}S

The ^{32}S data can be fitted relatively well up to 2.6 fm^{-1} using the Fermi model; the higher momentum transfers require one modification of shape (4). The resulting fit shows some systematic deviations from the data and has a χ^2 of 1.8 per degree of freedom.

The Gaussian distribution gives a very good fit to the low-q data up to 2.2 fm^{-1}; the remaining difference between experiment and low-q fit can be parametrized well using shape (4). The best fit has a χ^2 of 1.1 per degree of freedom and is shown in Fig. 7 together with best 3pG fit without modification. The best-fit charge distribution is given in Fig. 15, the parameters in Table V.

Summarizing, one can say that with one of the models used a satisfactory fit has been obtained for all three nuclei. The fact that ^{28}Si can be fitted with 3pG without further modification implies that the amplitude of oscillations in $\rho(r)$, with a wavelength similar to the ones found in S and ^{24}Mg, are smaller than 10% than the amplitudes found in S

TABLE V. Best-fit parameters for ^{24}Mg (3pF), ^{28}Si, and S (3pG).

^{24}Mg	$C = 3.192 \pm 0.034$ fm $Z = 0.604 \pm 0.006$ fm $W = -0.249 \pm 0.02$	(3pF)	$A = -0.076$ $q = 2.49$ fm^{-1} $p = 0.51$ fm^{-1}
^{28}Si	$C = 1.954 \pm 0.09$ fm $Z = 2.076 \pm 0.01$ fm $W = 0.286 \pm 0.012$	(3pG)	
S	$C = 2.543 \pm 0.09$ fm $Z = 2.191 \pm 0.01$ fm $W = 0.160 \pm 0.012$	(3pG)	$A = 0.021$ $q = 2.83$ fm^{-1} $p = 0.50$ fm^{-1}

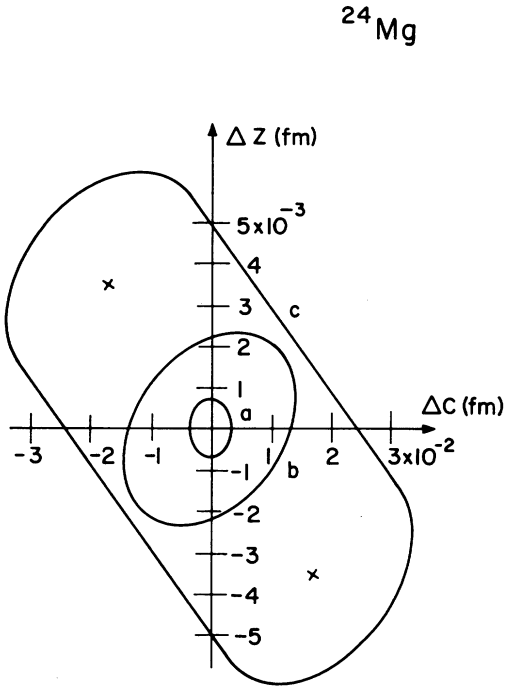

FIG. 16. Error contours for the basic parameters of ^{24}Mg. The ellipses are the projections of the error ellipsoid in the c-z plane due to energy uncertainty (curve a), double statistical error (curve b), shift due to absolute normalization (x) and sum (curve c).

and ^{24}Mg. This shows that in ^{28}Si the relative contributions of the $2s$ and $1d$ shells happen to be such that $\rho(r)$ is practically flat for radii smaller than 1.5 fm. The χ^2 values do not always approach the number of degrees of freedom. This is essentially due to some residual systematic deviations which were too small to justify the introduction of further modifications. For ^{28}Si a contribution of ~15 in the value of χ^2 comes from a few points in the first diffraction minimum, where the fits always give cross sections ~6% lower than experimental values. For ^{24}Mg the two points at highest momentum transfer give an important fraction to the total χ^2; however, they contain too little information to warrant a more complicated $\Delta\rho$. For every nucleus one of the two models used gives a considerably higher χ^2; the two charge densities can therefore not be compared directly since one must be excluded. A comparison of the densities is nevertheless useful, since it gives an estimate of the sensitivity of the fits to details of $\rho(r)$. In the center, where the difference 3pF – 3pG is always the largest, 3pF yields systematically higher values for the charge density. The maximum central density difference observed for the three nuclei occurs for ^{24}Mg and is ~3% of $\rho(0)$. Another systematic difference is visible in the rms radii, which for the Fermi model are ~0.01 fm greater than for 3pG.

One property of the charge distribution that might be expected to depend strongly on the model chosen is the tail of the density ($r > 4$ fm). Whereas the Fermi model cases obviously can give an exponential tail, the densities from the Gaussian model would be expected to drop off more rapidly. An inspection of the best-fit densities in the region $0.1\rho(0) < \rho < 0.001\rho(0)$ (i.e., $4.5 < r < 7$ fm) does not support this idea: both densities give an almost exponential tail with densities that differ very little. The reason lies in the very pronounced influence of the parameter w, which, in light nuclei, essentially acts on the tail. The parameter w is negative for 3pF and positive for 3pG. It serves to compensate the not-fast-enough, or

TABLE VI. Parameters for Fermi distributions.

	Present work	Mainz results	
^{24}Mg	$C = 3.192 \pm 0.034$ fm $Z = 0.604 \pm 0.006$ fm $W = -0.249 \pm 0.02$	$C = 3.08 \pm 0.03$ fm [a] $Z = 0.591 \pm 0.018$ fm $W = -0.14 \pm 0.03$	Ref. 8
^{28}Si	$C = 3.239 \pm 0.026$ fm $Z = 0.574 \pm 0.006$ fm $W = -0.149 \pm 0.015$	$C = 3.30$ fm $Z = 0.545$ fm $W = -0.18$	Ref. 9 [b]
S [b]	$C = 3.441 \pm 0.034$ fm $Z = 0.624 \pm 0.006$ fm $W = -0.213 \pm 0.014$	$C = 3.53$ fm $Z = 0.61$ fm $W = -0.26$	Ref. 10 [b]

[a] Statistical errors only.
[b] Natural isotopic composition.

TABLE VII. The rms radii in fm for ^{24}Mg, ^{28}Si, and S.

	Present work	Muonic x-ray result [a]	Other electron scattering results
^{24}Mg	2.985 ± 0.03	3.01 ± 0.03 [b]	2.97 ± 0.09 [a,c] 3.07 ± 0.088 [d,e]
^{28}Si	3.106 ± 0.03	3.086 ± 0.02 [b]	3.04 ± 0.09 [c] 3.08 ± 0.04 [d,f] 3.06 [a,g]
S	3.239 ± 0.03	3.244 ± 0.02 [b]	3.18 ± 0.09 [c] 3.12 [h] 3.23 ± 0.07 [i]

[a] Natural isotopic composition.
[b] Reference 27.
[c] Reference 3.
[d] Statistical errors only.
[e] Reference 8.
[f] Reference 9.
[g] Reference 7.
[h] Reference 5.
[i] Reference 10.

too-fast, drop-off incuded by the exponential term in Eq. (3). In the region $4.5 < r < 7$ fm, which still has a measurable influence on the cross sections, the tail is consequently practically the same for both models.

The errors in the parameters are the consequence of the statistical fluctuations and the systematic uncertainties in the experimental data. The statistical errors are obtained by computing the error matrix. The systematic error, which is mainly due to uncertainties in the absolute normalization, is obtained by varying the hydrogen calibration by 3% and refitting the data. An additional $\pm 0.1\%$ has to be taken into account in all length parameters (e.g., c and z) due to the uncertainty in the incident energy. As an example, the results of the error calculation are presented in Fig. 16. The ellipses shown are the projections of the error ellipsoid in c, z, w onto the c-z plane. The inner ellipse is due to the 0.1% uncertainty in the incident energy; the middle ellipse is due to twice the statistical error; the crosses give the effect of an over-all normalization change of $\pm 3\%$; the outermost curve gives the total uncertainty due to the above three sources.

The errors in fitting the parameters in $\Delta\rho(r)$ are mainly due to the statistical fluctuations; the contribution due to the systematic uncertainty is comparatively negligible. The accuracy for fixed c, t, and w is such that the amplitude is determined to about $\pm 10\%$, the wavelength to $\pm 1\%$, and the decay constant to $\pm 12\%$.

The errors in the rms radii quoted in Table II are due mainly to the normalization uncertainty; from fits to the data of similar precision for other nuclei[26] and for the 3pG-3pF comparison the model dependence of the rms radius can be estimated to $\pm 0.5\%$.

In Table VI the parameters of the 3pF distributions are compared to the ones obtained at $q \leq 2.1$ fm^{-1} at Mainz.[8-10] It should be kept in mind that the 3pF model does not give an optimal fit to the present data for ^{28}Si and ^{32}S.

In Table VII the rms radii obtained are listed together with results obtained by electron scattering and muonic x-ray studies.[27]

In the above analysis the contribution of dispersion corrections to the (e, e') cross sections has been neglected. No theoretical calculations concerning the intermediate excitation of nuclear states are available for the nuclei considered here. For ^{40}Ca, where several calculations exist, the dispersion corrections lead to a change of $\rho(r)$ of the order of 0.5% for radii smaller than 5 fm.[28] The magnitude of this change is comparable to the uncertainty of $\rho(r)$ due to the systematic errors in the data discussed above. These corrections are much smaller, for example, than the $\Delta\rho(r)$ used to fit the high-q data. The rms radius of ^{40}Ca changes by less than 0.1% when correcting the data with the calculated dispersion effects.

V. DIFFERENCES IN CHARGE DISTRIBUTIONS

In Fig. 15 the best-fit charge distributions are displayed together with the densities of ^{16}O and ^{40}Ca, the lightest and heaviest members of the s-d shell. Both these densities come from recent high-momentum-transfer work[26,1] ($q \leq 3.9$ and 3.4

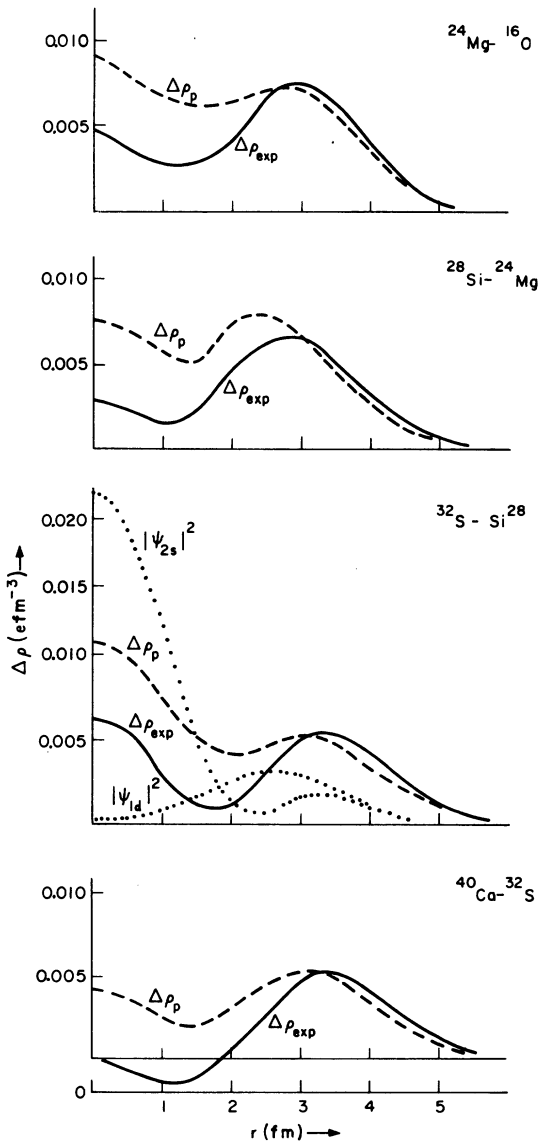

FIG. 17. Experimental differences in charge distributions ($\Delta\rho_{exp}$), and differences corrected for change of core density ($\Delta\rho_p$).

fm^{-1}, respectively). The densities reveal quite a pronounced structure apart from the general increase of radius with atomic number. The variation in the shape of $\rho(r)$ in the s-d shell are so rapid due to the two shells with very different wave functions being filled. In this section we will discuss the comparison of the experimental (phenomenological) charge density distributions for these five nuclei.

The experimental differences of charge distributions $\Delta\rho_{exp}$, are presented in Fig. 17. For ease of comparison, $\Delta\rho_{exp}$ has been divided by a factor of 2 in the cases of the pairs ^{40}Ca-^{32}S and ^{24}Mg-^{16}O. An inspection of Fig. 17 indicates that the difference between the central charge densities of ^{28}Si and ^{32}S is only 0.008 $e\,fm^{-3}$; if the assumption of the whole $2s$ shell being filled between ^{28}Si and ^{32}S were valid, it would suggest a value of $\Delta\rho(0)$ about five times larger. The difference between ^{28}Si and ^{24}Mg, which is about 0.005 $e\,fm^{-3}$ at $r = 0$ fm, indicates that a noticeable part of the $2s$ shell is already being filled there (the d protons contribute very little to the density at radii smaller than 1 fm). If we assumed that the $2s$ shell were empty in the case of ^{24}Mg and ^{16}O, then ^{24}Mg should have a smaller value of $\rho(r)$ at $r = 0$ fm than ^{16}O, since the increasing radius of the potential from ^{16}O to ^{24}Mg would imply a reduction of the charge density at the center; the contrary is observed experimentally.

Due to the dependence of the nuclear potential well radius on the mass number, the $\Delta\rho_{exp}$ do not give directly the charge distribution of the added protons. The difference due to the increase of the core radii can be estimated, however, within the harmonic-oscillator framework.

For every pair of nuclei shown in Fig. 17 the charge densities of the lighter partner have been calculated using the oscillator parameters of the two nuclei. These oscillator parameters have been determined by requiring the density of the two nuclei to fit the experimental rms radii. Then the difference of the two densities represents roughly the part of $\Delta\rho_{exp}$ not due to the charge distribution of the added proton, but rather the change due to the general increase of the nuclear

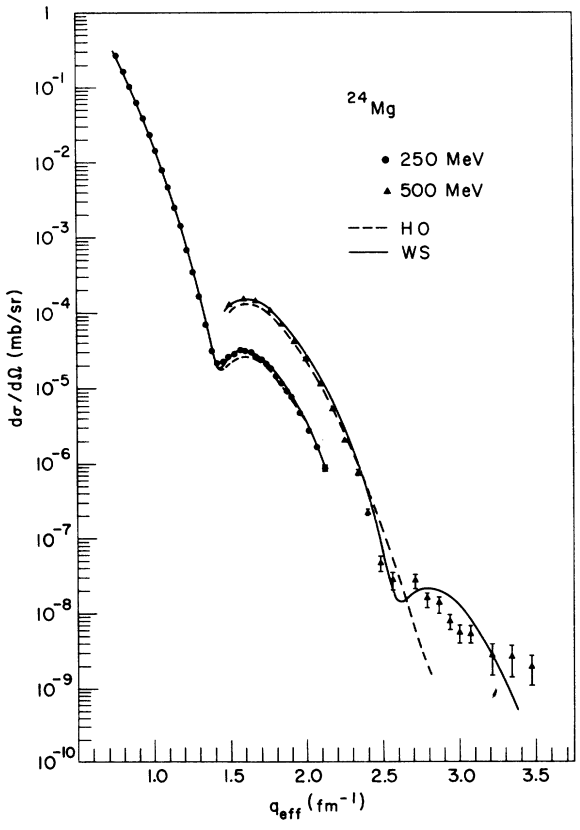

FIG. 18. Experimental cross sections of ^{24}Mg compared with calculated curves using the harmonic-oscillator model (HO) and a Woods-Saxon model (WS).

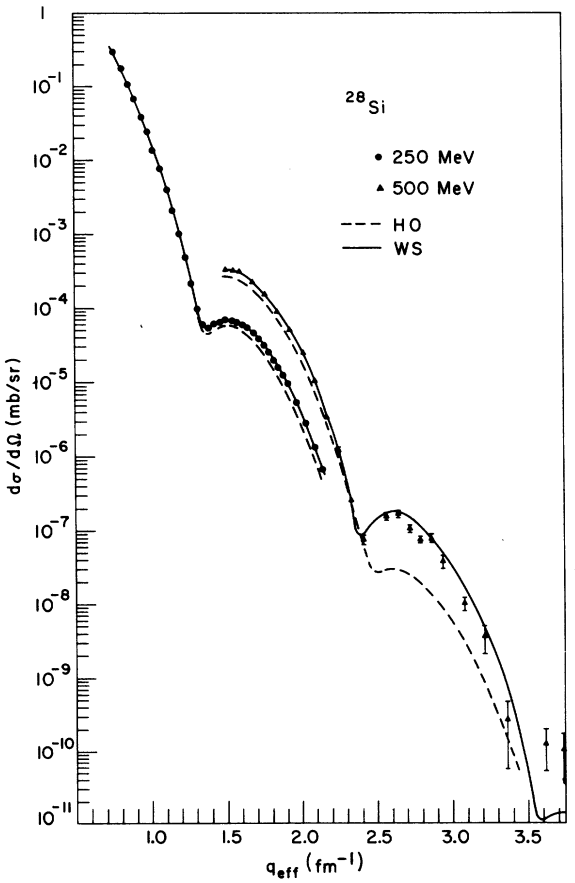

FIG. 19. Experimental cross section of ^{28}Si compared with calculated curves using the HO and WS models.

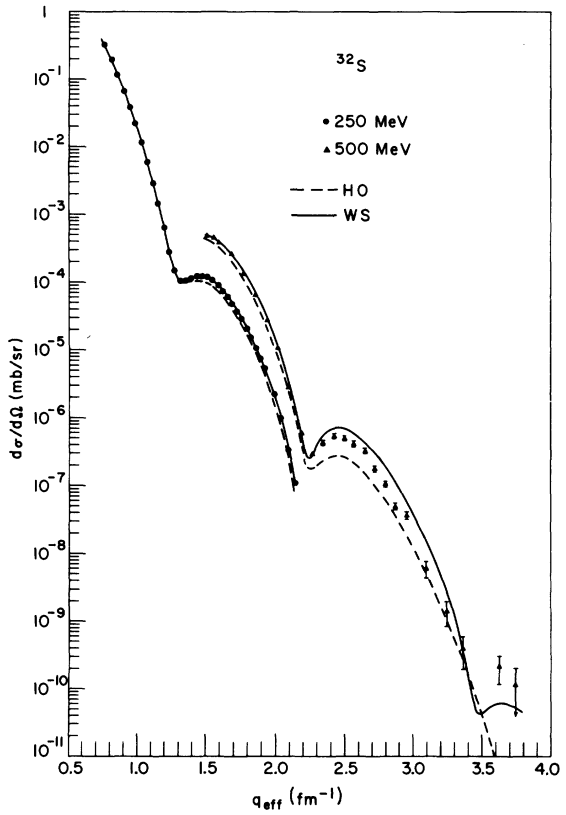

FIG. 20. Experimental cross sections of ^{32}S compared with calculated curves using the HO and WS models.

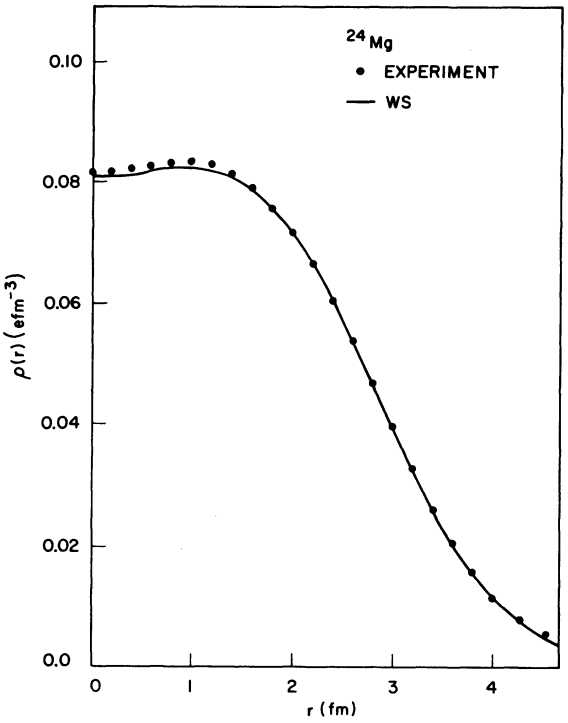

FIG. 21. Phenomenological $\rho(r)$ (dots) of ^{24}Mg compared with calculated curve using the WS model.

potential well radius. This difference has been subtracted from $\Delta\rho_{exp}$ to produce the curves $\Delta\rho_p$ given in Fig. 17. $\Delta\rho_p$ should in this crude approximation represent the distribution of the added protons.

In Fig. 17 the distribution of one $1d$ and one $2s$ proton have been indicated also. A comparison of these two possible contributions to both $\Delta\rho_p$ and $\Delta\rho_{exp}$ shows very clearly the separate effects of the added $2s$ and $1d$ shell protons through the two peaks at $r = 0$ fm and $r \simeq 3$ fm. Consequently, this experiment demonstrates qualitatively that the filling of the $2s$ shell is spread out over a rather large region of A. Within the approximation used to obtain $\Delta\rho_p$ one could then make an interpretation in terms of the shell-model occupation number (smo) of the $2s$-$1d$ shell rather easily. However, it was preferred to extract it in a more quantitative way as described in the following section.

VI. SHELL-MODEL CALCULATIONS

In order to examine the proton distribution in the nucleus in a more realistic way, a better independent-particle shell model must be used. The

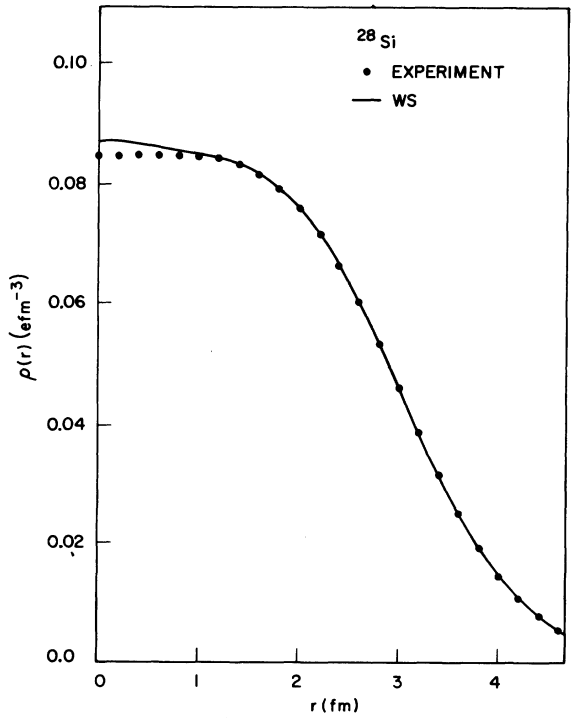

FIG. 22. Phenomenological $\rho(r)$ (dots) of ^{28}Si compared with calculated curve using the WS model.

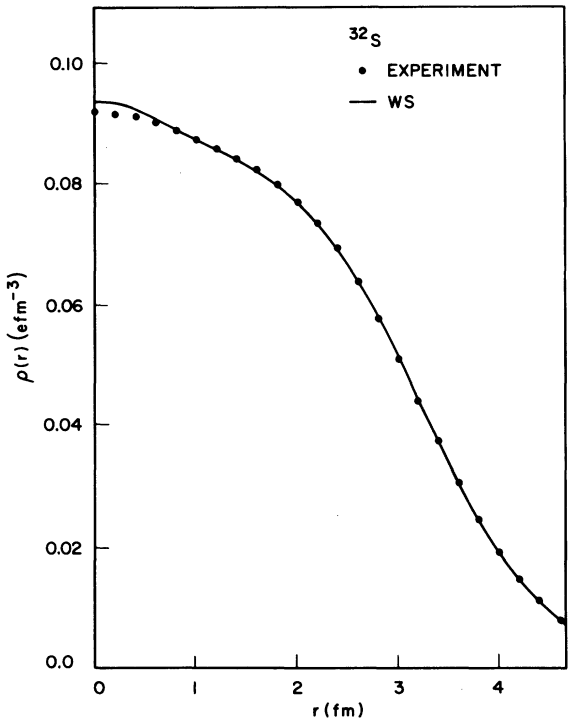

FIG. 23. Phenomenological $\rho(r)$ (dots) of ^{32}S compared with calculated curve using the WS model.

actual nuclear potential was chosen to be of the Woods-Saxon form

$$V(r) = \frac{V_0}{1+\exp[(r-A)/T]} \ , \tag{6}$$

with the well depth V_0, half radius A, and the surface thickness parameter T treated as free parameters. The effects of the spin-orbit interaction and the Coulomb potential were also included. The choice of the spin-orbit potential proves not to be critical for the present calculation; omitting it completely would change the densities at radii <4 fm by less than 0.5%. The influence of the exact shape of the Coulomb potential is also minor. The charge distribution responsible for the Coulomb potential has therefore been approximated by a uniform distribution.

The $2s$-$1d$ occupation number was also treated as a free parameter; without this degree of freedom, totally unacceptable fits resulted. The $1s$ and $1p$ shells were assumed to be filled and the experimental separation energies as given by $(p,2p)$ experiments[29] were used as a constraint (for ^{24}Mg, the $1d_{5/2}$ energy; for ^{28}Si and ^{32}S, the $2s_{1/2}$ energy). The possibility of protons being in the $1d_{3/2}$ shell was not considered explicitly, since the present analysis does not allow any statement to be made about the relative $1d_{5/2}$-$1d_{3/2}$ occupation number due to the similarity of the radial wave functions.

With the four parameters mentioned above (the well depth, the surface thickness, the half radius, and the $2s$-$1d$-shell occupation number) and one constraint (the separation energy), the charge distribution $\rho_{WS}(r)$ was calculated[30] by folding in the proton size. The center-of-mass correction necessary for the fixed WS-well calculation was performed as described in Ref. 26.

Reasonably good fits were obtained with χ^2 values between 3.4 and 11.6 per degree of freedom. The best fits to the experimental data are shown in Figs. 18 to 20. The best $\rho_{WS}(r)$ for ^{24}Mg, ^{28}Si, and S are presented in Figs. 21 to 23, respectively. The parameters found are given in Table VIII.

The $2s$-shell occupation numbers obtained are 0.6, 0.9, and 1.4 for Mg, Si, and S, respectively. They confirm the more qualitative impression

TABLE VIII. Experimental separation energy, best-fit Woods-Saxon-model parameters.

	^{24}Mg	^{28}Si	^{32}S
V_0 (MeV)	62.09	62.74	56.89
T (fm)	3.838	3.975	3.986
A (fm)	0.72	0.72	0.73
V_{so} (MeV)	10.0	10.0	10.0
$E_{p,2p}$ (MeV)	11.65	13.20	9.1
Z_{2s}	0.6	0.9	1.4
χ^2/degree of freedom	19.6	3.4	9.2
r_{rms} (fm)	3.024	3.109	3.253

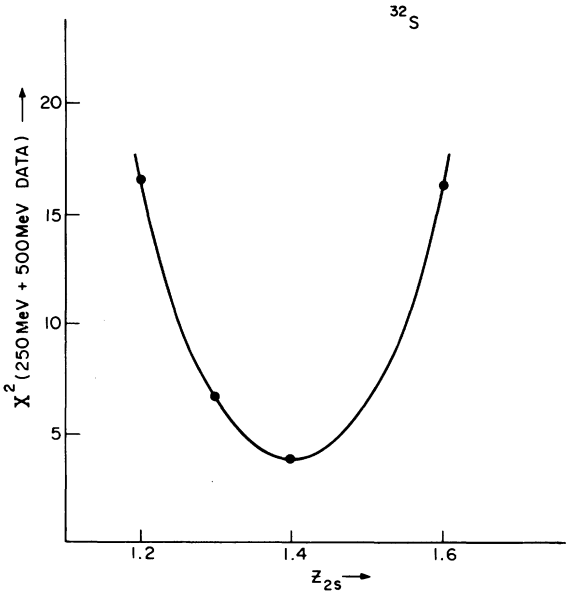

FIG. 24. The dependence of χ^2 on Z_{2s} for ^{32}S, all other parameters adapted at every point for minimum χ^2.

from Fig. 17 of a very gradual filling of the $2s$ shell. In Fig. 24 the dependence of χ^2 on the $2s$-shell occupation number Z_{2s} for ^{32}S is plotted; for every given Z_{2s} all other parameters were adjusted for minimum χ^2. Figure 24 indicates that a fit to the electron scattering data is very sensitive to the $2s$ occupation. An error of $\sim\pm 0.1$ can be assigned to Z_{2s} according to Fig. 24. The sensitivity to Z_{2s} is due to the high-momentum-transfer points which allow a determination of the central charge density of the nucleus; $\rho(r\sim 0$ fm) depends on Z_{2s} in an essential way, and only to a minor extent on the wave function of the $1s$ state.

The results concerning the $2s$-shell occupation numbers can be compared to the values obtained from stripping and pickup reactions by means of sum rules[31,32] which relate the spectroscopic factors to the occupation numbers. A recent analysis[33] of this type gives the experimental $2s$-shell occupation numbers of 0.19, 0.79, and 1.5 for ^{24}Mg, ^{28}Si, and ^{32}S, respectively; the values calculated in Ref. 33 with the projected Hartree-Fock method are 0.39, 0.70, and 2.0. The agreement of the present results, typically 0.6, 0.9, and 1.4, with the occupation numbers deduced from pickup reactions is surprisingly good except for ^{24}Mg, where the high value of $\rho_{exp}(0)$ seems hard to reconcile with an occupation number for the $2s$ protons as low as 0.19; it is conceivable, however, that one of the essential $l=0$ transitions in the pickup reactions used to arrive at the number $Z_{2s}=0.19$ has not yet been observed. A recent $(d,{}^3\mathrm{He})$ experiment on ^{24}Mg (Ref. 34) yields a considerably higher Z_{2s}, 0.46; this value is compatible with our result of 0.6, considering the uncertainties of the two determinations.

When calculating the charge density from the WS wave functions, the contribution of the neutrons[35] has been neglected. As a consequence of the present relatively poor knowledge of the neutron charge form factor, this contribution, which amounts to 0.5–1% of $\rho(r)$ for radii <5 fm, is quite uncertain. It can be neglected without influencing the above results because larger deviations between experiment and fit (deviations which are due to the oversimplifications inherent in the WS model) have been tolerated.

It should be noted that the Woods-Saxon model used is somewhat questionable in this region of A, since the nuclei are generally considered to be deformed. The fact that ^{24}Mg, presumably the most strongly deformed of the three nuclei, gave the highest value of χ^2 might be taken as an indication of this. On the other hand, the apparent surface thickness parameter for the WS well, which could be considerably larger with an intrinsic deformation, is almost constant for ^{24}Mg, ^{28}Si, and ^{32}S and is not particularly large ($\sim$0.72 fm).

VII. CONCLUSIONS

The elastic scattering cross sections of ^{24}Mg, ^{28}Si, and ^{32}S have been analyzed by several models. First, two phenomenological charge distributions have been deduced; second, the nuclear Woods-Saxon potential has been used to parametrize the charge distributions. This WS model is much less phenomenological considering the range of applicability in nuclear physics that prompts the use of this WS potential. Moreover, the constraint on the separation energy together with the spin-orbit force taken from other experiments ensures that not only the radial wave functions but, roughly, also the single-particle energies are correct. The phenomenological models allow a good fit of the data due to the sufficient flexibility of the parametrizations chosen. The Woods-Saxon potential does not reproduce the data with a comparable quality. This is a consequence of the reduced flexibility of the potential and the various shortcomings of the extreme single-particle model used. Three available parameters, the fourth being used to fulfill the energy constraint, is too restrictive a set to explain the data over such an extensive momentum transfer region with the desired accuracy. The deviations of experiment and fit visible at high q explain well the difference between ρ_{WS} and ρ_{phen} in the center region; this can be shown by parametrizing the form factor difference, as has been done for the phenomenological analysis, and calculating the corresponding density change.

For the most precise extraction of the charge distribution one therefore will have to rely on the phenomenological model. The WS fits made here have, apart from the information obtained on the potential parameters and the $2s$ occupation numbers, their merits also for the determination of $\rho(r)$: There is little ambiguity in the high frequency components of the density function, since the shape of these oscillations around the mean density are given by the wave functions of the different shells, which, for the present purpose, are quite independent of the potential used. The close agreement of empirical and WS densities indicates that the remaining ambiguity in the high frequency components (due to the lack of measurements at higher momentum transfer) has no serious consequences for the phenomenological density. The explanation lies in the fact that the momentum transfer region reached in the present experiment is sufficiently high to make visible the main features of the oscillation in $\rho(r)$ due to shell structure. One obviously could add to the

empirical densities an oscillation having a wavelength ≤ 1.5 fm without changing the χ^2 of the best fit. But taking the WS calculation (and the same is true for a Hartree-Fock calculation) as a guide for the amplitude of the high frequency components that might occur one finds that they would be of the order of a few percent of $\rho(0)$.

The main feature that emerges from the WS fits is the gradual filling of the $2s$ shell. This fact, evident also from the empirical charge densities, is known from pickup reactions; however, only with the very high q data measured here has it been possible to extract an occupation number from (e, e) experiments. The agreement of the two completely independent determinations, one of which depends on the $2s$ wave function in the center of the nucleus, the other one on the wave function in the tail, is very encouraging.

ACKNOWLEDGMENTS

The authors wish to express their deep appreciation to Professor Robert Hofstadter for his continued support and encouragement throughout this project. Thanks go to Professor T. W. Donnelly, Professor J. S. McCarthy, Professor J. D. Walecka, and Professor G. E. Walker, who were kind enough to discuss many of the theoretical and experimental aspects of this work, and to Professor J. Heisenberg for the use of his elastic phase-shift computer program. Thanks also go to operating crew of the Stanford Mark III linear electron accelerator and the staff of the High Energy Physics Laboratory.

†Work supported in part by the National Science Foundation under Grants Nos. NSF GP 28299 and NSF GP 22880 and by the Swiss National Science Foundation.

[1]J. B. Bellicard, P. Bounin, R. F. Frosch, R. Hofstadter, J. S. McCarthy, F. J. Uhrhane, M. R. Yearian, B. C. Clark, R. Herman, and D. G. Ravenhall, Phys. Rev. Lett. 19, 9 (1967).

[2]L. R. B. Elton, S. J. Webb, and R. C. Barrett, in *Proceedings of the Third International Conference on High Energy Physics and Nuclear Structure, Columbia University, 1969*, edited by S. Devons (Plenum, N. Y., 1970).

[3]R. H. Helm, Phys. Rev. 104, 1466 (1956).

[4]G. R. Bishop and G. A. Proca, J. Phys. Radium 22, 541 (1961).

[5]R. Lombard, P. Kossanyi-Demay, and G. R. Bishop, Nucl. Phys. 59, 398 (1964).

[6]G. A. Savitskii, N. G. Afanasev, I. S. Gulkarov, V. M. Khvastunov, A. A. Khomich, and N. G. Shevchenko, Yad. Fiz. 7, 1181 (1968) [transl.: Sov. J. Nucl. Phys. 7, 705 (1968)].

[7]G. A. Savitskii, N. G. Afanasev, I. S. Gulkarov, V. D. Kovalev, A. S. Omelaenko, V. M. Khvastunov, and N. G. Shevchenko, Yad Fiz. 8, 648 (1968) [transl.: Sov. J. Nucl. Phys. 8, 376 (1969)].

[8]P. Junk, Ph.D. thesis, Universität Mainz, 1970 (unpublished).

[9]G. Mulhaupt, Ph.D. thesis, Universität Mainz, 1970 (unpublished).

[10]H. Hultzsch, Ph.D. thesis, Universität Mainz, 1970, (unpublished).

[11]K. L. Brown, Rev. Sci. Instrum. 27, 959 (1956).

[12]L. R. Suelzle, Ph.D. thesis, Stanford University, 1967 (unpublished).

[13]J. Heisenberg, J. S. McCarthy, R. Parks, and I. Sick, High Energy Physics Laboratory Technical Note No. 68-16, 1968 (unpublished).

[14]R. Hofstadter, in *Proceedings of the International Conference on Instrumentation for High Energy Physics* (Interscience, New York, 1961), p. 310.

[15]F. A. Bumiller, High Energy Physics Laboratory Report No. 257, 1962 (unpublished).

[16]L. R. Suelzle and M. R. Yearian, in *Proceedings of the International Conference on Nucleon Structure, Stanford University, 1963*, edited by R. Hofstadter and L. I. Schiff (Stanford U. P., Stanford, California, 1964). 1964).

[17]Targets were obtained from Oak Ridge National Laboratory.

[18]G. C. Li, I. Sick, J. D. Walecka, and G. E. Walker, Phys. Lett. 32B, 317 (1970).

[19]T. Janssens, R. Hofstadter, E. B. Hughes, and M. R. Yearian, Phys. Rev. 142, 922 (1966).

[20]H. L. Crannel and L. R. Suelzle, Nucl. Instrum. Methods 44, 133 (1966).

[21]H. L. Crannell, Phys. Rev. 148, B1107 (1966).

[22]L. W. Mo and Y. S. Tsai, Rev. Mod. Phys. 41, 205 (1969).

[23]L. Lapikas, A. E. L. Dierperink, and G. Box, Nucl. Phys. A203, 609 (1973).

[24]The phase shift program was written by J. Heisenberg.

[25]D. R. Yennie, D. G. Ravenhall, and R. N. Wilson, Phys. Rev. 95, 500 (1954).

[26]I. Sick and J. S. McCarthy, Nucl. Phys. A150, 631 (1970).

[27]G. Backenstoss, S. Charalambus, H. Daniel, H. Koch, G. Poelz, H. Schmitt, and L. Tauscher, Phys. Lett. 25B, 547 (1967).

[28]I. Sick, Nucl. Phys. A (to be published); also C. Toepffer and D. Drechsel, Phys. Rev. Lett. 24, 1131 (1973); W. F. Lin, Phys. Lett. 39B, 447 (1972); and R. Rosenfelder, Nucl. Phys. A216, 477 (1973).

[29]M. Riou and C. Ruhla, Prog. Nucl. Phys. 11, 195 (1970); H. Tyren, S. Kullander, O. Sundberg, R. Ramachandrau, P. Isacsson, and T. Berggren, Nucl. Phys. 79, 321 (1966).

[30]The computer program (WOODY) was due to T. W. Donnelly and G. E. Walker, private communication.

[31]J. B. French and M. H. Macfarlane, Nucl. Phys. 26, 1613 (1956).

[32]M. H. Macfarlane and J. B. French, Rev. Mod. Phys. 32, 567 (1960).

[33]B. Castel, I. P. Johnstone, B. P. Singh, and J. C. Parikh, Nucl. Phys. A157, 137 (1970).

[34]E. Krämer, G. Mairle, and G. Kaschl, Nucl. Phys. A165, 353 (1971).

[35]W. Bertozzi, J. Friar, J. Heisenberg, and J. W. Negele, Phys. Lett. 41B, 408 (1972).